

Publications

---

10-27-2002

## An Observation of a Fast External Atmospheric Acoustic-gravity Wave

J. H. Hecht

*Space Science Applications Laboratory, The Aerospace Corporation*

R. L. Walterscheid

*The Aerospace Corporation*

Michael P. Hickey Ph.D.

*Embry-Riddle Aeronautical University, hicke0b5@erau.edu*

R. J. Rudy

*Aerospace Corporation*

A. Z. Liu

*University of Illinois at Urbana-Champaign*

Follow this and additional works at: <https://commons.erau.edu/publication>



Part of the [Atmospheric Sciences Commons](#)

---

### Scholarly Commons Citation

Hecht, J. H., Walterscheid, R. L., Hickey, M. P., Rudy, R. J., & Liu, A. Z. (2002). An Observation of a Fast External Atmospheric Acoustic-gravity Wave. *Journal of Geophysical Research: Atmospheres*, 107(D20). <https://doi.org/10.1029/2001JD001438>

This Article is brought to you for free and open access by Scholarly Commons. It has been accepted for inclusion in Publications by an authorized administrator of Scholarly Commons. For more information, please contact [commons@erau.edu](mailto:commons@erau.edu).

## An observation of a fast external atmospheric acoustic-gravity wave

J. H. Hecht,<sup>1</sup> R. L. Walterscheid,<sup>1</sup> M. P. Hickey,<sup>2</sup> R. J. Rudy,<sup>1</sup> and A. Z. Liu<sup>3</sup>

Received 30 October 2001; revised 24 April 2002; accepted 17 May 2002; published 29 October 2002.

[1] In November 1999 a new near-IR airglow imaging system was deployed at the Starfire Optical Range outside of Albuquerque, New Mexico. This system allowed wide angle images of the airglow to be collected, with high signal to noise, every 3 seconds with a one second integration time. At approximately 1000 UT on November 17, 1999, a fast wavelike disturbance was seen propagating through the OH Meinel airglow layer. This wave had an observed period of  $\approx 215$  seconds, an observed phase velocity of  $\approx 160$  m/s and a horizontal wavelength of  $\approx 35$  km. This phase velocity is among the fastest yet reported using an imager viewing the OH Meinel bands, while the wave period is among the shortest. Simultaneous Na lidar wind and temperature data from 80 to nearly 110 km altitude allow the intrinsic properties of the wave to be calculated. The *Einaudi and Hines* [1970] WKB approximation for the acoustic-gravity wave dispersion relation was used to calculate the wave's intrinsic properties. Using this approach indicates that the observed disturbance was an external acoustic wave in the 90 to 107 km altitude region and an external gravity wave at other altitudes between 80 and 90 km. Using model atmospheric data for altitudes below and above this altitude regime indicates that the wave is essentially external everywhere except perhaps in narrow regions around 80 and 105–110 km. This is confirmed using a more exact full-wave model analysis. The observations and model results suggest that this wave was not generated in the troposphere and propagated up to the mesosphere, but rather near 100 km altitude where it was possibly generated by a Leonids meteor. *INDEX TERMS*: 0310 Atmospheric Composition and Structure: Airglow and aurora; 0342 Atmospheric Composition and Structure: Middle atmosphere—energy deposition; 3332 Meteorology and Atmospheric Dynamics: Mesospheric dynamics; 3384 Meteorology and Atmospheric Dynamics: Waves and tides

**Citation:** Hecht, J. H., R. L. Walterscheid, M. P. Hickey, R. J. Rudy, and A. Z. Liu, An observation of a fast external atmospheric acoustic-gravity wave, *J. Geophys. Res.*, 107(D20), 4444, doi:10.1029/2001JD001438, 2002.

### 1. Introduction

[2] There are a number of atmospheric waves with periods from a few seconds to a few hours which can be present in the atmosphere. These can be categorized as either internal waves which are characterized by having a vertical phase variation, or external (evanescent) waves which have no vertical phase variation. Depending on the wavelength and period, internal waves can additionally be classified as an acoustic wave, which has an intrinsic period below the acoustic cut-off, typically less than a few minutes, or a gravity wave, which has a period above the Brunt-Vaisala period, typically about 5 minutes [Beer, 1974]. A particular external wave that is hydrostatic and propagates horizontally at the speed of sound is known as a Lamb wave [Beer, 1974].

[3] The most striking feature in most airglow images is the presence of what appears to be nearly monochromatic wave fronts that commonly propagate from one edge of the image to the opposite edge and have been referred to as bands [Taylor *et al.*, 1995; Clairemidi *et al.*, 1985]. Their characteristics have been studied extensively by several groups [Taylor *et al.*, 1995; Swenson *et al.*, 1999; Nakamura *et al.*, 1999; Smith *et al.*, 2000]. Typically these waves have horizontal wavelengths from 20 to 50 km, observed phase speeds from 10 to 100 m/s and periods from several minutes to an hour. These waves have almost always been classified as internal atmospheric gravity waves, originating in the troposphere and propagating up to the upper mesosphere and lower thermosphere region [see, e.g., Taylor *et al.*, 1987; Taylor and Hapgood, 1988; Taylor *et al.*, 1997; Nakamura *et al.*, 1999].

[4] Probably the least studied aspects of airglow images are the wave structures that appear with observed periods less than the Brunt-Vaisala period which is nominally between 4 and 5 minutes [Beer, 1974]. While such waves have been observed [Frey *et al.*, 2000; Smith *et al.*, 2000; Taylor *et al.*, 1997; Nakamura *et al.*, 1999; Swenson *et al.*, 1999; Isler *et al.*, 1997] the exact nature of these waves was not always well determined because of uncertainties in the background wind and temperature structure.

<sup>1</sup>Space Science Applications Laboratory, The Aerospace Corporation, Los Angeles, California, USA.

<sup>2</sup>Department of Physics and Astronomy, Clemson University, Clemson, South Carolina, USA.

<sup>3</sup>Department of Electrical and Computer Engineering, University of Illinois, Urbana, Illinois, USA.

[5] For more than 30 years ionosondes have reported periodic variations with periods in the 1–20 minute range [see, e.g., *Georges*, 1968, and references therein; *Jones*, 1970, and references therein]. Often such variations are seen, with periods near 3 minutes, during times that are associated with thunderstorms. *Jones* [1970] performed steady state calculations of acoustic, gravity and Lamb wave normal modes and concluded that these 3-minute waves are generated by a coupling between the Lamb wave normal mode and the first acoustic wave normal mode. Thus, acoustic waves generated in the troposphere are believed to be measured by ionosondes from thermospheric altitudes (above 150 km). This suggests that such waves may be observable in the upper mesosphere. However, in normal operation most imagers do not have the temporal resolution to search for waves with such short periods. Typical integration times are a few tens of seconds and typical sample times are on the order of a minute or more between measurements of the same emission feature since several emission features are typically sampled [see *Taylor et al.*, 1995].

[6] In November 1999 a new near-IR airglow camera was placed at the Starfire Optical Range in Albuquerque New Mexico. One mode of operation of this camera is to image the 1.55 to 1.7  $\mu\text{m}$  wavelength region which includes bright OH Meinel (OHM) band emissions from the OHM (3,1) and (4,2) vibrational bands. This allowed images to be obtained every three seconds with one second integration times and signal to noise ratios for single pixels of nearly 200 to 1. Moreover during this period the University of Illinois Na wind and temperature lidar was operating providing high vertical resolution wind and temperature data from 80 to nearly 110 km.

[7] Around 1000 UT (Universal Time) on November 17, 1999 during the period of the Leonids meteor shower, but one day before the peak, fluctuations in the airglow brightness, as recorded by our camera, were observed with a period of  $\approx 215$  s. Examination of the images revealed the presence of a wavelike structure with an observed phase velocity of  $\approx 160$  m/s and a horizontal wavelength of  $\approx 35$  km. The observed phase velocity is faster than any previously reported wave of which we are aware.

[8] The remainder of this paper describes the airglow observations and the associated lidar wind and temperature data. Both a WKB analysis following *Hines* [1960] and *Einaudi and Hines* [1970], and a full-wave model analysis [*Hickey et al.*, 1997, 1998] are used to determine the nature of this wave. The results of the analysis suggests that the wave was generated in the upper mesosphere or lower thermosphere and propagated downwards rather than originating in the troposphere and propagating upwards.

## 2. Experimental Instrumentation and Technique

### 2.1. Near-IR Camera

[9] A new near-infrared camera was located at the Starfire Optical Range in November, 2000. A future publication will describe the camera in detail but a brief overview is given next. This camera combines a custom, wide-angle lens with a 256 by 256 HgCdTe detector array to provide images over an  $\approx 73 \times 73$  degree region of the sky. The detector, a NIC-MOS3 device developed by Rockwell International, is identical to the devices by the same name that are currently

operating on the Hubble Space Telescope. The lens, which consists of 10 separate AR coated elements, provides an  $f/5$ , telecentric output. The output is passed through a 4-position filter wheel to select two OHM lines, the nearby continuum, and an open position. These photons are then passed into a cryogenic enclosure where a 6-element re-imaging system (also AR coated and optimized for transmission between 1.2 and 1.8  $\mu\text{m}$ ) reduces the image size to the 1 cm dimensions of the array. At the detector surface the optics are operating at  $f/1.3$ . Within the cryogenic camera cell is a broadband astronomical “H” filter (1.55–1.75  $\mu\text{m}$ ) that transmits the output of the external filter. This “H” filter is sandwiched with a custom blocking filter that moves the red edge to 1.70  $\mu\text{m}$  and considerably reduces the thermal background. In order to facilitate remote observations for extended periods when no servicing is possible, the entire optics/detector train is cooled by a commercial cryo-cooler. The device uses the free-expansion of gas (Joule–Thompson effect) to provide an essentially vibrationless cooling head. A thermal switch links the cooling head to the detector mount that, in turn, is connected through a thermal insulator to the optics. This arrangement provides for the two very different temperatures needed to optimize performance while minimizing the cooling requirements ( $T(\text{detector}) = 83$  K,  $T(\text{optics}) = 139$  K). Two narrow-band filters (FWHM = 4 nm) isolate the first two OHM 4-2 vibrational band P-branch rotational lines (at 1.6026 and 1.6124  $\mu\text{m}$ , while a third filter at 1.5750  $\mu\text{m}$  samples the continuum. The latter filter is centered so it will not pass any OHM or O<sub>2</sub> IR (0,1) band airglow [*Baker et al.*, 1975]. A fourth filter position is open, allowing a spectral range (1.55–1.7  $\mu\text{m}$ ) determined by the internal filters to be imaged. The detector electronics (clocks, biases, preamps, A/Ds) provide a range of integration times (0.1–1000 seconds) at low read noise ( $\leq 30$  e). Because the OHM (4,2) band brightness is almost 100 kRy [see, e.g., *Krassovsky*, 1962], the signal to noise (S/N) can be quite high since each of the rotational lines have brightness values close to 10 kRy. For a 5 second exposure on a single rotational line there is a measured 70:1 S/N in a single pixel that spans about 0.5 by 0.5 km at the OHM layer. In the open filter position mode, where the signal can be 8 times greater, a 1 second integration gives a S/N of about 200:1. Thus, this camera allows a very fine detailed study of features with very short temporal and spatial scales.

### 2.2. Na Wind and Temperature Lidar

[10] Nearly simultaneous temperature and wind data were obtained from the University of Illinois Na Wind/Temperature lidar system [*Bills et al.*, 1991; *Gardner and Papen*, 1995] co-located at Starfire Optical Range. This lidar technique derives wind and temperature by using peak and two wing frequencies to probe the shape of the Na D<sub>2</sub> absorption line, which are functions of wind (Doppler shift) and temperature (thermal broadening). By taking advantage of the Starfire 3.5 m telescope this lidar system can measure winds and temperatures at better than 100 m vertical resolution with a few minute integration time. For this work the lidar obtained densities every 24 m but these are averaged and the resultant 96 m bins are used.

[11] In a normal mode of operation the lidar takes profiles in one of five positions; in the vertical, and 10 degrees off vertical due north, south, east, or west. Typically, these are

taken sequentially and meridional or zonal winds are obtained by first subtracting opposite winds in pairs (north-south and east-west) in order to eliminate the vertical component and then dividing the result by twice the sine of 10 degrees. Temperatures can be obtained from any of the profiles.

[12] However, on this night the lidar was in a mode where it could be used to search for Leonids meteor trails. Thus, the positions were not done sequentially and the lidar was often in a single position for several approximately 24 second integration periods. For this work the data over these consecutive scans at a given direction, and the closest set of scans from the opposite direction, were used in the subtraction. Because the period of interest is around 10.0 UT the scans that were used were taken between 9.86–9.89 UT towards the south, 9.98 to 10.02 UT towards the north, 9.90 to 9.93 UT towards the west, and 10.04 to 10.07 UT towards the east. To increase the signal to noise the data were smoothed over 10 points or 960 m.

[13] Temperature data were the average of profiles from 9.89 to 10.10 UT. These data were also smoothed over 960 m.

### 2.3. Model Analysis

[14] Hickey's full wave model is described in detail by *Hickey et al.* [1997, 1998, 2000, 2001], while the WKB approximation dispersion relations are described in detail by *Einaudi and Hines* [1970]. Briefly, the full-wave model solves the complete linearized equations of continuity, momentum and energy for a compressible, viscous, and thermally conducting atmosphere with arbitrary altitude variation in a basic state thermal structure, and is used to calculate the upward propagation of waves in the terrestrial atmosphere. The full-wave model, unlike a WKB model, rigorously accounts for wave reflection. Details of the model and its application to the upward propagation of gravity waves in Earth's atmosphere are given by *Hickey et al.* [1997, 1998]. Acoustic wave propagation in Earth's atmosphere is described by *Hickey et al.* [2001], and gravity wave propagation in Jupiter's atmosphere is described by *Hickey et al.* [2000].

[15] For the full-wave model simulations discussed here the upper boundary was set to 400 km altitude. The lower boundary was specified to suit in some respects the particular characteristics of wave solutions associated with transient sources of short duration (e.g., thunderstorms, bolides). With such sources one would not expect the solution to be affected by the ground, except perhaps far from the source. This is due to the time it takes the waves to communicate the effects of the ground to the high-altitude region. For the particular problem of interest here, the lack of communication between the high-altitude source and the ground is mimicked in the full-wave model by placing the lower boundary at –200 km altitude (that is, 200 km below the ground), and by implementing a sponge layer between the lower boundary and the ground. Wave solutions are set to zero at the lower boundary, although sensitivity tests revealed that the wave solutions above the ground were insensitive to the actually lower boundary condition because of the sponge layer. This specification of the lower boundary precludes ground effects as required for this problem, especially for the high-altitude source. This decoupling is not quite so clear for the source located at 20 km, but the solution is evanescent virtually everywhere

and this alone will act to reduce the sensitivity to the ground for the low-altitude source (and also the high-altitude source). A test with the lower boundary at the ground (not shown) and no sponge layer gave results for both sources that did not differ significantly from the results with the sponge layer.

[16] The basic state winds are the Na lidar winds, shown below, smoothly joined to those obtained from the Horizontal Wind Model (HWM-93) [*Hedin et al.*, 1996] as follows. For the region 25 km below the lowest altitude of the lidar data (that lowest altitude being designated  $z_{\min}$ ), a weighted mean,  $u(z)$ , of the lidar wind at  $z_{\min}$ ,  $u_{\text{lidar}}(z_{\min})$ , and HWM winds,  $u_{\text{hwm}}(z)$ , was calculated using

$$u(z) = (1 - w(z)) * u_{\text{hwm}}(z) + w(z) * u_{\text{lidar}}(z_{\min})$$

for  $(z_{\min} - 25\text{km}) < z < z_{\min}$  and where the weighting,  $w(z)$ , is defined as

$$w(z) = (z - z_{\min} + 25)/25$$

A similar procedure was applied to the joining of the winds in the 25 km region above the highest altitude of the lidar data. Afterwards, a smoothing spline was fit to all points to ensure that the first and second derivatives of the winds varied smoothly across the fairing regions.

[17] The basic state temperature data uses Na lidar temperature data, shown below, smoothly joined in a similar manner to the winds, to MSIS-90 model data [*Hedin*, 1991] for the regions above and below the lidar altitude regime. For the temperature data, however, the fairing region is about 10 km. This was because the mean temperature is already smoother than the winds, and is also more monotonic.

[18] For both the winds and temperatures the measured data from 80 to 108 km are smoothed over approximately 2.5 km. The raw temperature data indicate the presence of a superadiabatic region where the temperature lapse rate exceeds 9.5 K/km. The 2.5 km smoothing reduces this to below 9.5 K/km. Although such a superadiabatic region cannot be a permanent feature of the atmosphere, it nevertheless represents the state of the atmosphere as experienced by the observed high-frequency wave (and the modeled wave) at the time of the observations. The superadiabatic lapse rate was probably caused by a large amplitude gravity wave or tide that significantly perturbed the atmosphere. Importantly, this perturbation would have occurred on a time scale significantly longer than that associated with the observed high-frequency wave. Therefore, to see if this large negative temperature gradient has an effect, a smaller smoothing is also used in some full-wave model runs in order to preserve the superadiabatic lapse rate.

[19] For the full-wave model simulations discussed here the upper boundary was set to 350 km altitude. The lower boundary was set to –200 km and a sponge layer was implemented at this lower boundary in a similar manner to that used in a study of gravity waves in Jupiters atmosphere by *Hickey et al.* [2000]. Sponge layers at the bottom and top of the model domain insure against spurious wave reflection from the lower and upper boundaries. The sponge layers are applied in both the momentum and



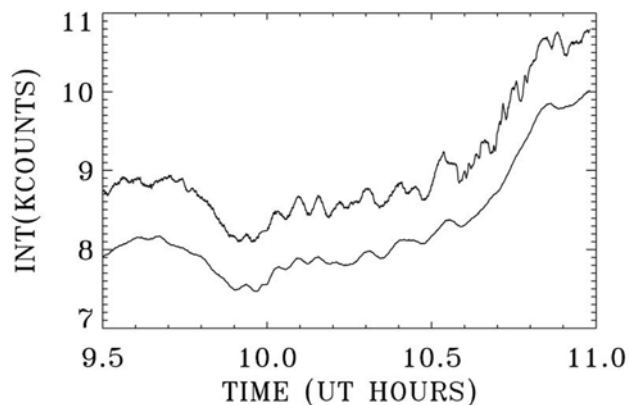


**Figure 1.** Two time series taken on 11/17/99 of the OH Meinel intensity, in kilocounts, versus time, in UT hours. The bottom curve is derived by using a 10 by 10 km boxcar over the central portion of each image and plotting the intensity as a function of time with images being obtained every 3 seconds. The top curve, which is displaced upwards by 500 counts for clarity, shows the same time series except a 1 km boxcar smooth was used on each image, and the resultant time series was three point smoothed.

energy equations. The expression for the Rayleigh friction coefficient is

$$K_R = \omega_u e^{(z-z_u)/H_u} + \omega_l e^{(z_l-z)/H_l}$$

where here  $\omega$  is the intrinsic wave frequency, subscripts u and l refer to the upper and lower sponge layers,

respectively,  $z$  is altitude, and  $H$  is a damping scale height. In all calculations we use  $H_u = 20$  km,  $H_l = 50$  km,  $z_l = -200$  km, and  $z_u$  equals the upper boundary height (350 km). This was done to remove reflection from the lower boundary, allowing us to simulate high altitude sources in the model without wave solutions being dominated by standing waves between the ground and the source.

### 3. Results

#### 3.1. Airglow Observations

[20] Figure 1 shows two time series of OH intensity as a function of Universal Time (UT) taken on 11/17/99. UT is 7 hours ahead of local time. The bottom curve is derived by using a 10 by 10 km boxcar over the central portion of each image and plotting the intensity as a function of time with images being obtained every 3 s. The top curve, which is displaced upwards by 500 counts for clarity, shows the same time series except a 1 km boxcar smooth was used on each image, and the resultant time series was three-point smoothed. In the period around 10 UT there is a series of features separated by, on average,  $215 \pm 10$  seconds. Since at 0959 UT the imager switched into taking dark images with the shutter closed, only the feature before that period (954 to 958 UT) and the three prominent features from 1000 to 1012 UT were used to calculate the average separation in time. The amplitude of the largest fluctuation is about 2% of the mean.

[21] During this period a movie of consecutive images shows wavefronts moving rapidly through the field of view. Figure 2 shows an image at two different contrasts of the difference between an image taken at 100315 (10 hours,

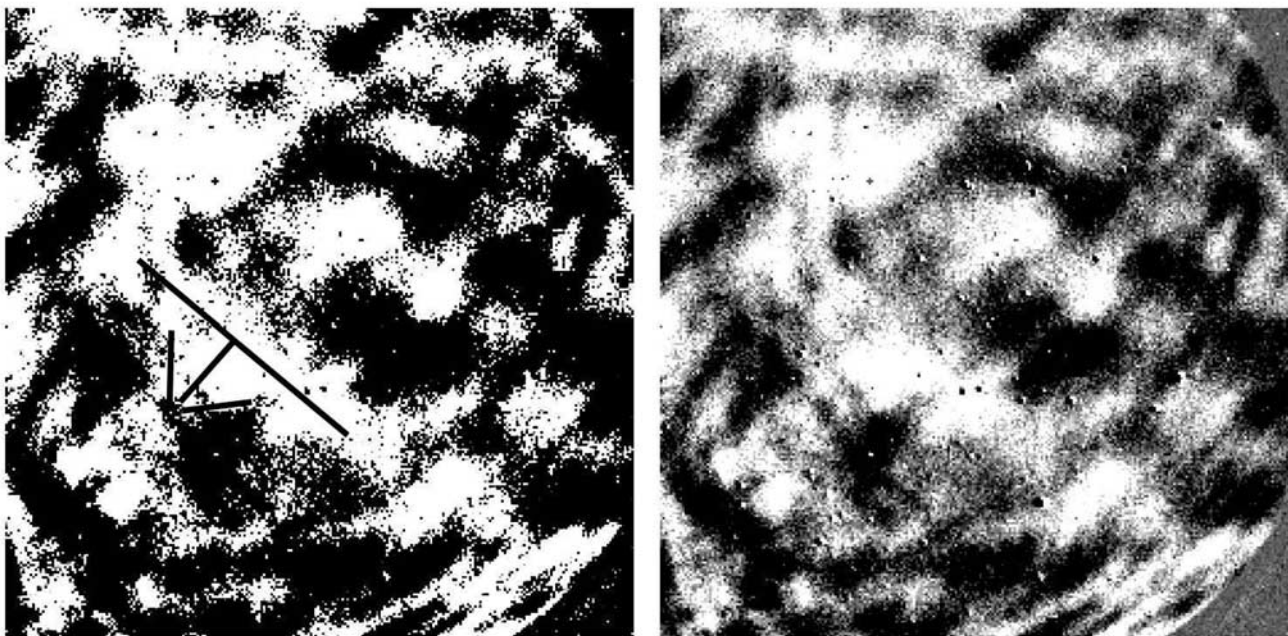


**Figure 2.** Two images, at two different contrasts, of the difference between a 1 second exposure taken at 100315 and 100122UT. The contrasts were adjusted to emphasize the presence of the 35 km wave discussed in the text (left image) and other features (right image). In each image north is on top and east is to the left. In the left image the arrow points in the direction of motion of the phase fronts. The field of view is approximately  $73 \times 73$  degrees and a single pixel towards the center is about  $0.5 \times 0.5$  km.

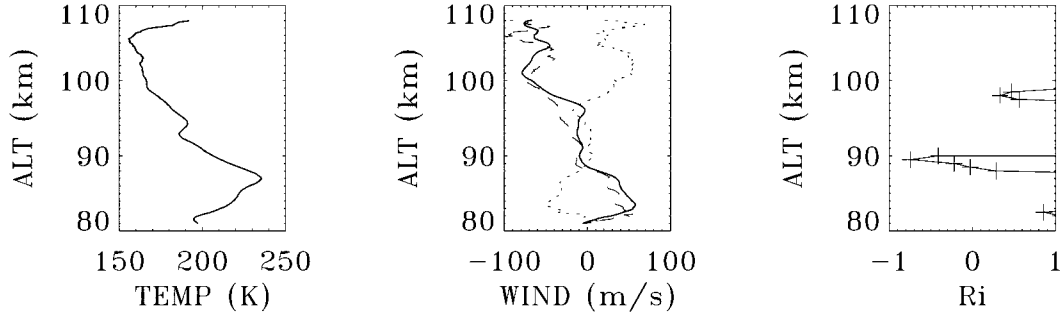


**Figure 3.** (left) The lidar temperature data as a function of altitude at the approximate time of the image data shown above. The derivation of these data and the data in the other two panels are described in the text. (middle) Wind data as function of altitude from the lidar. The solid line plot is in the direction of the wave. The long-dashed line is in the zonal direction. The short-dashed line is in the meridional direction. (right) The Richardson number as a function of altitude calculated from the lidar data.

3 minutes, and 15 seconds) UT and one taken at 100122 UT. The separation was chosen to be about one-half of the average period. Such a difference will emphasize the features near 215 s while suppressing the background long period features. The features causing the 215 s period fluctuations have a horizontal wavelength of  $\approx 35$  km with an uncertainty of  $\approx 2$  km in determining this value. The features move from the approximate direction of the northwest (upper right) to the southeast (lower left). Following *Garcia et al.* [1997] the curvature of the field was taken into account when calculating the horizontal wavelength at an assumed altitude of 90 km. The observed phase velocity is  $\approx 160 \pm 10$  m/s which is larger than any such velocity reported in the recent comprehensive studies of *Taylor et al.* [1997], *Swenson et al.* [1999], *Nakamura et al.* [1999], or *Smith et al.* [2000]. While the observed period of the wave is less than the nominal 4-minute acoustic cut-off intrinsic period suggesting that, for small background wind speeds, this is an acoustic wave, the phase velocity is well below the sound speed of  $\approx 300$  m/s expected at 90 km. Since a freely propagating internal acoustic wave has a phase speed above the speed of sound [*Beer, 1974*] this suggests that the observed wave is evanescent.

[22] The right hand panel of Figure 2 shows this difference image at lower contrast. In addition to the 35 km horizontal wavelength wave there are many other wave-fronts present. Most have shorter horizontal wavelengths and usually seem to occur perpendicular to the fast wave.

### 3.2. Temperature and Wind Observations

[23] Figure 3 shows the wind and temperature data from the lidar. The temperature plot shows a large amplitude wave, which is modifying the background temperature, producing a maximum at 230 K just below 90 km and a minimum near 160 K at around 105 km. The temperature gradient is quite steep between these two altitudes, especially in the region between 87 and 93 km, and actually exceeds the adiabatic lapse rate of 9.5 K/km around 90 km. The zonal and meridional winds are given in the middle panel along with the derived wind in the direction of the wave, which is taken as towards 30 degrees east of south.

While the wind velocities can be quite high they are still well below the wave speed.

[24] The stability of the atmosphere is typically given by the Richardson number (Ri) defined as

$$Ri = \frac{(g/T)(dT/dz + g/C_p)}{(dU/dz)^2} \quad (1)$$

where,  $g$  is the acceleration of gravity,  $T$  is the atmospheric temperature,  $g/C_p$  is the adiabatic lapse rate,  $dU/dz$  is the magnitude of the vertical wind shear, and  $z$  is altitude [*Richardson, 1920; Beer, 1974; Gossard and Hooke, 1975*]. The numerator is the square of the Brunt-Vaisala frequency. When Ri is less than zero due to a temperature lapse rate which exceeds the adiabatic lapse rate, the atmosphere is considered to be convectively unstable. When Ri is between 0 and 0.25, typically due to the presence of a large wind-shear, the atmosphere is considered to be dynamically unstable. Although the limit at 0.25 has not been rigorously shown to be valid, and there is still some debate about this criterion, it is still generally accepted as an indicator of a dynamical instability [see, e.g., *Gossard and Hooke, 1975; Hines, 1971*].

[25] Both instabilities lead to the formation of secondary structures. A dynamical instability leads to the formation of streamwise Kelvin-Helmholtz (KH) billows while a convective instability results in streamwise convective cells or span-wise vortices. While the basic nature of KH billows is well known [*Gossard and Hooke, 1975*], the span-wise convective instability has only recently been well characterized [*Fritts et al., 1997*] for the mesosphere and lower thermosphere using three dimensional modeling. *Hecht et al.* [1997] have observed these structures due to a convective instability and they often appear as short wavelength waves (with a spacing around 10 km) perpendicular to larger scale wave structures.

[26] The right-hand panel in Figure 3 shows the results of using these wind and temperature data to calculate Ri values which are negative in the region around 90 km, indicating a convectively unstable region. There is also a region around 97 km which is close to being dynamically unstable. Thus,

some of the smaller wavelength structures seen in Figure 2 where may be due to these instabilities.

### 3.3. WKB Model Analysis

[27] *Einaudi and Hines* [1970] applied the WKB approximation to study acoustic-gravity wave propagation through an atmosphere with a slowly varying background temperature. Since they used the symbol  $q$  to represent the vertical wavenumber, and because we are closely following their development in this paper we also use the symbol  $q$  to represent the vertical wavenumber. Although current convention uses  $m$  to represent the vertical wavenumber, our alternative use of  $q$  is used exclusively and self-consistently throughout and so should not cause confusion to the reader. Additionally, following their usage a dot over a symbol refers to a derivative with respect to altitude ( $z$ ). For the simple case of an isothermal atmosphere the vertical wavenumber of the atmosphere,  $q_0$ , is given by the following equation where we include the inertial frequency term following *Gossard and Hooke*, [1975].

$$q_0^2 = (2\pi/\lambda_z)^2 = \frac{(\omega_g^2 - \omega_I^2)(k^2)}{(\omega_I^2 - f^2)} + \frac{\omega_I^2}{C^2} - \frac{1}{4H^2}. \quad (2)$$

In equation (2),  $C$  is the speed of sound,  $H$  is the atmospheric scale height,  $\omega_I$  is the intrinsic frequency with respect to a frame of reference that moves with the background wind,  $k$  is the horizontal wavenumber derived from  $(2\pi/\lambda_h)$  where  $\lambda_h$  is the horizontal wavelength,  $\omega_g$  is the Brunt-Vaisala frequency given isothermally by  $(\gamma-1)^{1/2}g/C$  where  $\gamma$  is the ratio of specific heats, and  $f$  is the inertial frequency equal to  $2\Omega\sin(\phi)$ , where  $\phi$  is latitude and  $\Omega$  is the angular speed of the earth. For a given background wind velocity component,  $\bar{u}$ , in the direction of the wave, and an observed wave horizontal phase velocity,  $c$ , the Doppler shifted wave velocity ( $c - \bar{u}$ ) is equal to  $(\omega_I)(\lambda_h)/(2\pi)$  or simply  $(\lambda_h/\tau_I)$ . The observed phase velocity  $c$  is equal to  $\lambda_h$  divided by the observed period. Since for these data  $f$  is much smaller than the intrinsic wave frequency that term is ignored for the remainder of this discussion and thus

$$q_0^2 = (2\pi/\lambda_z)^2 = \frac{(\omega_g^2 - \omega_I^2)(k^2)}{(\omega_I^2)} + \frac{\omega_I^2}{C^2} - \frac{1}{4H^2}. \quad (2a)$$

which is the same as equation 23 of *Einaudi and Hines* [1970].

[28] When there is a temperature gradient, *Einaudi and Hines* [1970] give several equations for the derived vertical wavelength. For example equation (41) of their study gives

$$q^2 = q_0^2 + k\dot{\alpha}/(\alpha\beta) + (\dot{\alpha})^2/(4\alpha^2) - \ddot{\alpha}/(2\alpha) \quad (3)$$

for the three-dimensional velocity divergence. (In a nonisothermal atmosphere, different quantities may have different equations for  $q$  as discussed by *Einaudi and Hines* [1970].) Ignoring terms in  $(\dot{\alpha})^2$  and  $\ddot{\alpha}$  reduces (3) to

$$q^2 = q_0^2 + k\dot{\alpha}/(\alpha\beta) \quad (3a)$$

where

$$\alpha = \gamma Hk$$

and

$$\beta = \omega^2/(gk)$$

and the derivatives denoted by dots are with respect the altitude  $z$ . One of the conclusions of the *Einaudi and Hines* [1970] study was that for most practical cases ignoring the higher order derivatives is appropriate, since, if these become too significant then the WKB approximation breaks down and one can no longer associate  $q$  with a vertical wavenumber.

[29] Equation (3a) also reduces to the same form as (2a)

$$q^2 = \frac{(\omega_B^2 - \omega_I^2)k^2}{(\omega_I^2)} + \frac{\omega_I^2}{C^2} - \frac{1}{4H^2}$$

where

$$\omega_B^2 = \omega_g^2 + (g/T)\dot{T} \quad (4)$$

where  $\omega_B$  is the non-isothermal Brunt-Vaisala frequency.

[30] If  $q^2$  is greater than zero the wave has a vertical component of phase propagation and such waves are referred to as internal. These internal waves propagate vertically without any decrease of wave energy density with height. However, if  $q^2$  is less than zero the wave energy density decreases in a direction away from the source, it has no component of vertical phase propagation, and the wave is referred to as evanescent or external.

[31] To determine the properties of the observed wave, we use the atmospheric profiles discussed above which combine the measured, but smoothed, lidar data with model data appropriate to the November period. The results for the various values of  $q^2$  given in equations 2a, 3, and 3a are shown in Figure 4. The results for equation 2a, which uses  $\omega_g$  not  $\omega_B$ , show the wave to be strongly evanescent everywhere from 40 to 140 km. When the height variations in temperature are taken into account through equations 3, 3a, and 4 the wave still appears to be external everywhere except perhaps near 85 and 110 km where  $q^2$  gets close to zero.

[32] Compared to internal waves external waves have not been well studied and the WKB interpretation of  $q$  does allow some additional insights to be obtained about the nature of such waves. Figure 5 has four contour plots which show isopleths of  $q^2$  as a function of  $k$  and  $\omega$  as derived from equation 3. The isopleths of  $q^2$ , are plotted only for external waves ( $q^2 < 0$ ) and the X in the plots shows the location of the observed wave ( $k$  and  $\omega_I$ ) at four different altitudes, 85 km, 90 km, 105 km, and 107.5 km. There are two straight lines on each plot. One is horizontal at the Brunt-Vaisala frequency derived from equation 4. This would represent a buoyancy wave with zero horizontal group velocity. The other straight line is a diagonal and represents the dispersion relation for a Lamb wave.

[33] *Beer* [1974] discusses a wave called the characteristic surface wave whose dispersion relation satisfies

$$\omega^4 = (C\omega_B k)^2. \quad (5)$$



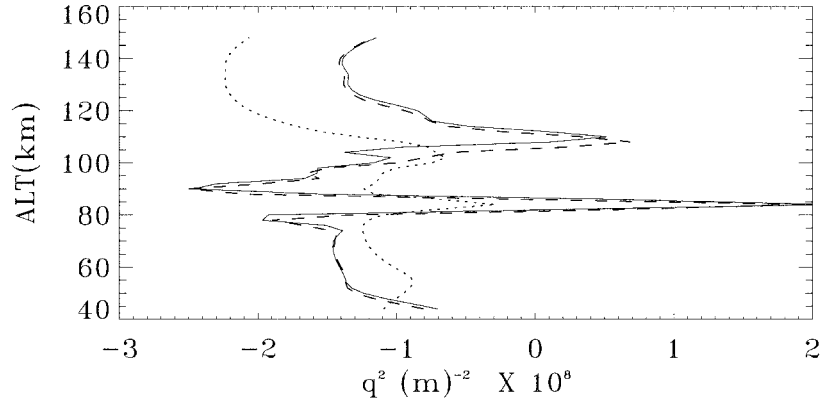


**Figure 4.** Plots of the square of the vertical wavenumber,  $q$ , as derived using the Einaudi and Hines WKB approximation assuming a horizontal wavelength of 35 km, an observed period of 215 s and using the measured lidar winds and temperatures (see text). The solid line uses equation 3, the dashed line uses equation 3a while the dotted line assumes an isothermal atmosphere and uses equation 2.

This represents a boundary between external acoustic waves and external gravity waves. Note that the three waves (Lamb, buoyancy, characteristic) meet at a single point which we refer to here as the triple point. The horizontal wavelength at that point is referred to here as the characteristic wavelength (CW) and its possible significance will be discussed below. The CW values at the three altitudes are also given on each plot.

[34] The observed wave, marked by the X, appears to be just in the internal gravity wave regime near 85 km, in the external acoustic wave regime at and above 90 km, and approaches the triple point at 107 km. In fact, the wave is essentially in the external acoustic wave regime from 87.5 to 107 km. Below 87.5 km the wave appears to be mainly in the internal gravity wave regime although near the triple point. Above 107 km the wave is internal although on the characteristic surface wave line.

### 3.4. Full-Wave Model Results

[35] The WKB analysis breaks down when the temperature gradients become large, greater than approximately 7 K/km Beer [1974]. This criterion certainly is met or exceeded in the altitude region above 105 km and thus a full-wave model analysis is needed to see how the WKB results are modified. Several model runs were made of the atmospheric response using the same basic state used in the WKB approach. Figure 6 shows results for two runs. Each assumes a wave with a 215 s period and with a horizontal wavelength of 35 km to simulate the observed wavelength. One places the wave source at 20 km altitude and the other places the wave source at 75 km altitude. All runs were normalized to reproduce the temperature of an appropriate magnitude so that when the airglow chemistry was applied the resultant perturbation in the integrated OH intensity was approximately 2% matching the characteristics of the observed wave.

[36] First, consider the results for the 20 km source altitude. The wave is external everywhere below 80 km. There is a narrow region between 80 and 85 km where the wave amplitude increases and decreases resembling a trapped wave. There is another similar but broader region which peaks near 110 km. The wave appears to be strongly evanescent above this region. For this source altitude the

peak response at around 80 km is nearly the same as at 110 km. The magnitudes of both peaks are less by about a factor of five than at 30 km. A run with the source at 20 km was also made for the temperature profile which preserves the superadiabatic lapse rate near 90 km. The results are almost identical to those shown.

[37] Runs were also made (not shown) with a source at 20 km altitude and with either a 30 or 40 km horizontal wavelength wave in order to bound the lower and upper limits to the observed wavelength. With the 30 km horizontal wavelength the peak at 80 km altitude is larger, by about a factor of three, than at 110 km altitude. Both are over an order of magnitude less than at 30 km altitude. When the horizontal wavelength is 40 km the peak at 110 km is about 50% larger than the one at 80 km altitude. These peaks are about a factor of two less than at 30 km.

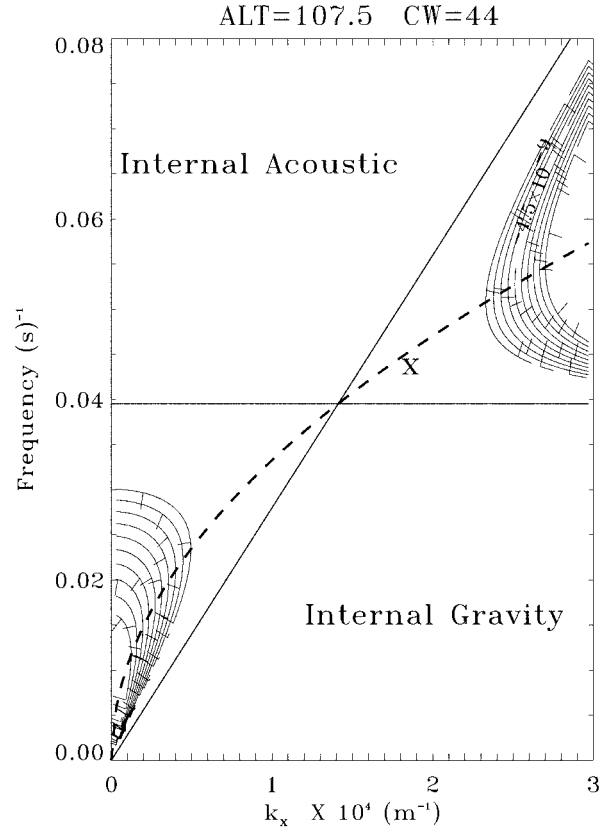
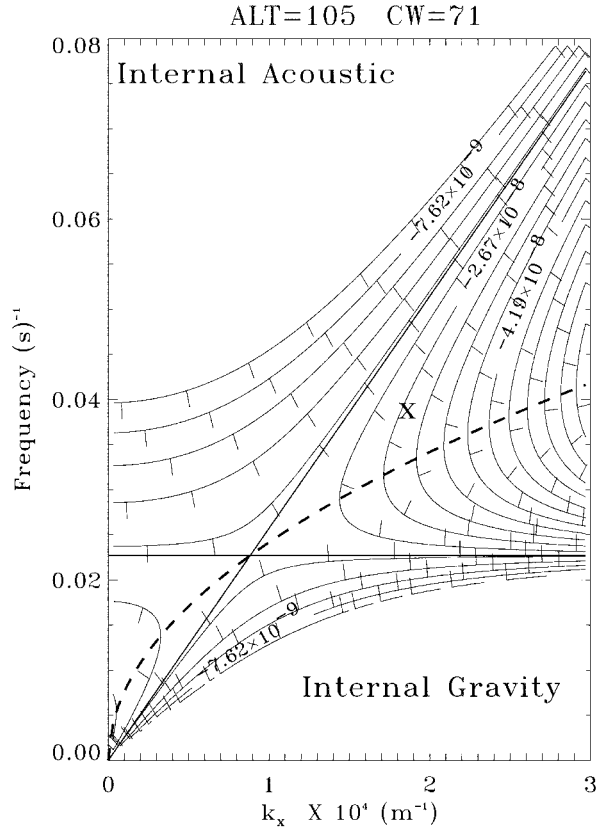
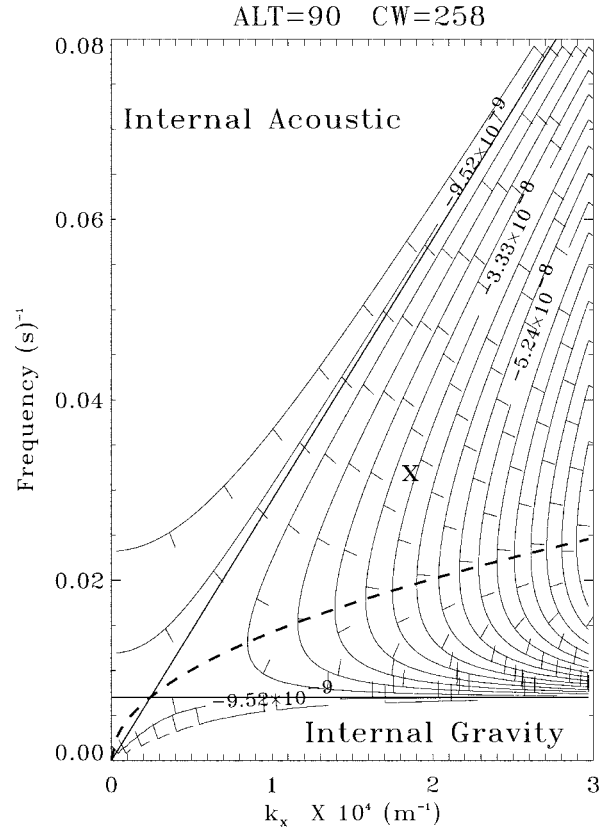
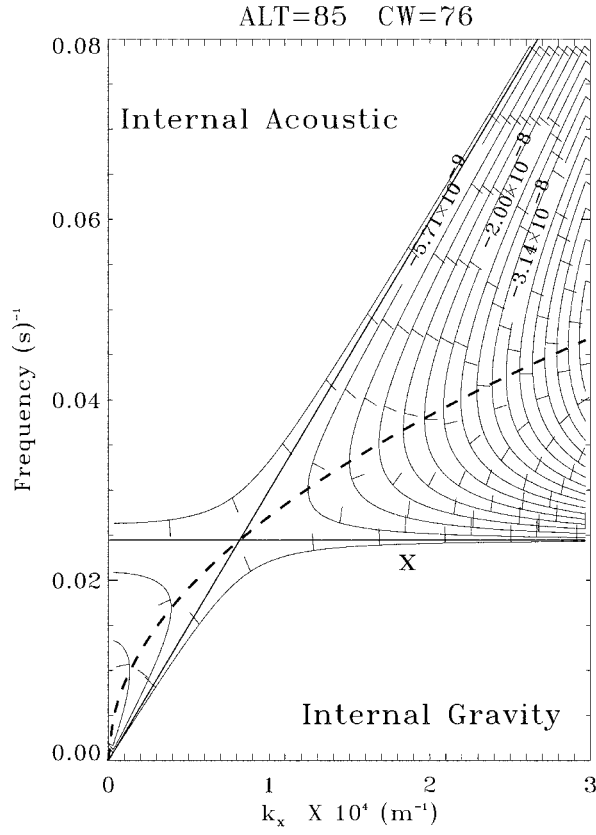
[38] The right hand panel of Figure 6 shows the results for a 75 km source altitude with a 35 km horizontal wavelength. Since the full-wave model analysis is steady-state, the source is always on, which is clearly different than a transient source such as a thunderstorm or a meteor. This illustrates that the response above the source is similar to that shown for the 20 km source altitude but there is little evidence of the wave below 60 km. This is what would be expected away from the source for a strongly external wave as it propagates vertically. These results suggest that a low altitude source is unlikely since it would have to be quite strong, while a high altitude source is possible. In this figure the Brunt-Vaisala period is also shown, and, intriguingly, the peaks in the temperature response seem to correspond to minima in this period.

[39] A source at 125 km altitude was also considered. These results (not shown) indicate a very large, nearly 100% temperature perturbation around 110 km when normalized to match the observed OH airglow response.

[40] These data can be used to derive a vertical wavenumber which has a real part ( $q_r$ ) derived from the vertical phase gradient and an imaginary part ( $q_i$ ) which indicates how the wave amplitude is increasing or decreasing with height. These quantities are defined as

$$q_r = \frac{\partial \phi_{T'}}{\partial z} \quad (6)$$





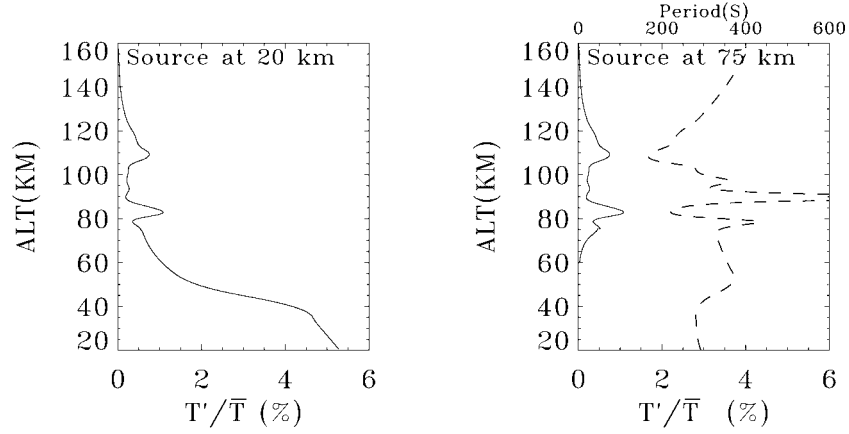


**Figure 6.** The ratio of the wave induced temperature perturbation  $T'$  to the average temperature  $\bar{T}$  as a function of altitude from the full-wave model analysis assuming a horizontal wavelength of 35 km. (left) The source in the full-wave model is at 20 km. (right) The source is at 75 km. In this panel the dashed line is the Brunt-Vaisala period in seconds divided by 100.

and

$$q_i = \frac{d[\ln(\bar{\rho}^{1/2}|T'|)]}{dz} \quad (7)$$

where  $\phi_T$  is the phase of the temperature perturbation and  $\bar{\rho}$  is the mean atmospheric density. At altitudes above the source the  $q_i$  is positive if the wave is growing, while it is negative if the amplitude is decreasing. For all these results the  $q_r$  is small compared to  $q_i$ . Note that in the dissipationless WKB approximation  $q$  is either purely real, when  $q^2$  is positive and the wave is internal, or purely imaginary, when  $q^2$  is negative and the wave is external. Figure 7 shows a comparison between  $q_i$  from the full-wave model and the imaginary part of the square root of  $q^2$  from the WKB approximation with both models using a 35 km horizontal wavelength. The WKB results are always negative if  $q^2$  is less than zero. Except for small regions around 80, 90, and 105–110 km the full-wave and WKB results are comparable and negative indicating that the wave energy is attenuating and the wave could be considered external. There are however two regions around 80 and 105–110 km where the full-wave results become clearly positive suggesting a region of wave growth. However, regions of wave reflection can produce similar results.

#### 4. Discussion

[41] There have been several earlier studies of normal modes of oscillation in the atmosphere for short period acoustic-gravity waves. In particular, *Balachandran* [1968]

analyzed acoustic-gravity wave propagation in a realistic atmosphere in order to explain ground-level pressure fluctuations seen from atmospheric intrusions such as meteors. The study found the existence of a number of modes for wave periods around 200 s. These atmospheric modes have maxima just above 100 km. One such mode, with a period of 216 s, was called the fundamental mode and is essentially a Lamb wave. However, gravity wave modes also existed with similar periods at similar altitudes. The shape of the modes strongly resemble the plots shown in Figure 6. *Jones* [1970] modeled the motions, with periods around 3 minutes, that are often seen in ionosonde data and which have been attributed to thunderstorms. This study showed that the atmosphere is highly resonant in the vicinity of the triple point region discussed earlier. Given the period of the observed wave it is likely that its excitation was related to a normal mode. Normal modes are the eigensolutions of a linear homogeneous system, are resonant and are the residual response to impulsive forcing. With respect to our observations, we are using the term mode to refer loosely to approximations to the normal modes set up by forcing of limited duration.

[42] The WKB analysis suggests the observed wave may resemble a buoyancy wave since at both 85 and 107.5 km the observed intrinsic wave frequency is very close to the Brunt-Vaisala frequency. We explored this somewhat by also performing full-wave model runs, with the source at 75 km, for waves with the following intrinsic characteristics at 107 km: (1) a wave at the triple point, (2) a wave near the triple point with a 40 km horizontal wavelength on the

**Figure 5.** (opposite) Four contour plots showing isopleths of  $q^2$  (contours of constant  $q^2$ ) as a function of the horizontal wave frequency horizontal wavenumber  $k$  derived from equation 3. Only regions where  $q^2$  are less than zero are contoured. The temperature adjusted Brunt-Vaisala frequency is shown as a horizontal solid line while the diagonal solid line represents the dispersion of a wave with the speed of sound, a Lamb wave. Regions where  $q^2$  are greater than zero are listed as internal gravity or acoustic regions depending upon whether  $\omega$  is below or above the Brunt-Vaisala frequency. In each plot the X represents the frequency and horizontal wavenumber of the observed wave. The dashed line represents the dispersion of the characteristic surface wave. For an isothermal WKB approximation this represents the boundary between external acoustic and external gravity waves. Four panels are shown at 85, 90, 105, and 107.5 km altitude. The horizontal wavelength of the triple point wave, referred to as the characteristic wavelength (CW) is also shown above each panel.

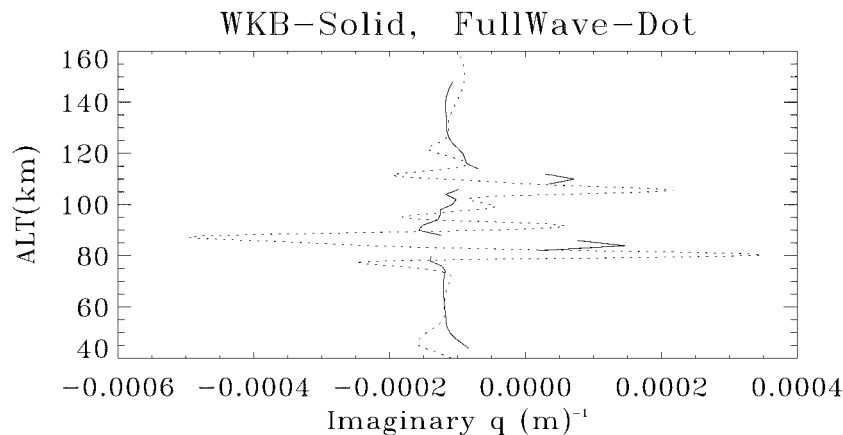


**Figure 7.** Plots of the imaginary part of  $q$  derived from the WKB approximation, equation 3a (solid line), versus altitude and the full-wave model  $q_i$  results (dotted line) versus altitude. For both models the horizontal wavelength is taken as 35 km.

Lamb wave curve, (3) a wave near the triple point with a 40 km horizontal wavelength at the Brunt-Vaisala frequency, and (4) two waves each at 21 km horizontal wavelength with a frequency at .05 and .07  $s^{-1}$  which are both displaced from the buoyancy or Lamb waves. With respect to the fractional temperature perturbation, the triple point (case one) and Lamb curve wave (case two) had the largest response at 110 km exceeding the response at 85 km by a factor of 4. The buoyancy type wave, case 3, behaved very much like the observed wave in Figure 6. The two waves at 21 km wavelength had much smaller responses at 110 km than at 80 km. Taken together these results suggest that the large response in the temperature perturbation seen near both 80–85 km and around 110 km is probably due to a buoyancy type oscillation that is excited because it is near the triple point, where our simulations and those of Jones [1970] indicate a preferred response. If the wave we observed was closer to the triple point too much energy would be found in the upper altitude near 110 km resulting in an inference of an unrealistically large source. If it was too far away from the triple point, not enough energy would be trapped and the response at 85 to 90 km would be too low.

[43] Whatever type wave is being excited (Lamb or Buoyancy), both the full-wave and WKB analysis suggest that the observed wave is external at altitudes below 80 and above 120 km. In fact except for some small regions around 110 and 80–85 km, where the positive  $m_i$  is probably related to the local excitation of the wave, the wave appears to be external everywhere else. This provides clues as to where the wave was generated.

#### 4.1. Where the Wave is Generated

##### 4.1.1. Troposphere

[44] If the wave were generated in the troposphere, the model results indicate that there would near 5% temperature fluctuations at 25 km. This translates into greater than 10 K temperature fluctuations. This seems quite large for a wave with an  $\approx 3$  minute period. Indeed, it is large compared to what has been measured using various techniques for the wave field including more energetic waves (see, for example, the GPS data from Tsuda *et al.* [2000]). At mid-latitudes

in the winter the GPS data from 20 to 30 km suggest fluctuations about 10 times smaller than what would be required to generate the wave.

[45] One possible lower atmospheric source would be a large thunderstorm. Observations of gravity waves generated by deep convection reveal wave temperature amplitudes in the lower stratosphere of  $\sim 2$  K [Alexander and Pfister, 1995]. Our modeling results described in section 3.4 suggests that these amplitudes are a factor of  $\sim 5$  too small to explain the airglow fluctuations observed here. Therefore, even if strong convection existed close to the time of the observations and within a distance on the order of 100 km from the imager the wave amplitudes in the mesopause region would have been too small to produce the observed airglow fluctuations. Additionally, we were present during the whole observing period and skies were completely clear. The weather records indicated that there were no large thunderstorms within a few hundred km of the observing site. Thunderstorms located further away could produce ducted waves. However they would require an even larger wave perturbation (above a 10K perturbation noted above) as energy is likely to be lost if the duct is leaky [Hecht *et al.*, 2001].

[46] Finally, stationary mountain waves (with a near zero observed phase speed in the troposphere) could not explain the high speed of the observed wave (with 160 m/s phase speed). Thus, it is difficult to reconcile our observations with a lower atmospheric (tropospheric) source.

##### 4.1.2. Upper Mesosphere/Lower Thermosphere

[47] Although the observation night at Starfire was one night before the main peak of the Leonids for 1999, there were a few persistent meteor trails similar to those reported previously and comparable to those seen on the following evening. Data from the 1998 Leonids observations over Starfire indicated that persistent Leonids meteor trails seem to occur between 90 and 100 km [Chu *et al.*, 2000]. One such trail was well-documented and was also found to produce infrasonic emission detectable on the ground [Revelle and Whitaker, 1999]. The bolide which produced this trail which, interestingly, occurred almost exactly one year before the present wave observation, was estimated to have an initial energy of about  $5 \times 10^9$  J and a radius of about 8 cm. The meteor exploded around 93 km.

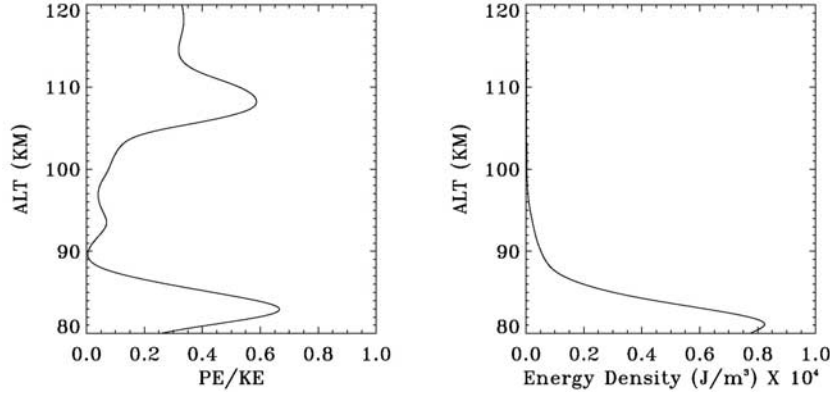


**Figure 8.** Plots of the wave energy and energy density calculated from the full-wave model using a 75 km source and assuming a horizontal wavelength of 35 km. (left) A plot of the ratio of the wave potential energy to the kinetic energy as a function of altitude. (right) The kinetic plus potential energy density of the wave, in  $\text{J/m}^3$ , as function of altitude.

[48] Our suggestion is that a significant amount of the energy deposited by a similar sized meteor excited acoustic-gravity wave oscillations. Some of this energy coupled into the excitation of either Lamb or Buoyancy waves around 80–85 or 105–115 km. The trapped wave energy propagated away from the source and we observed the evanescent tail of this wave connecting the two maxima as it passed over Starfire. Since the OH Meinel emission layer is nominally 10 km thick centered near 87 km we may be observing a wave that is internal in part of the layer (below 87 km) and external in part (above 87 km).

[49] We estimated the wave energy by assuming four 35 km wavelength crests and a 100 km horizontal extent; the latter is almost certainly an underestimate. We used the full-wave model results for the 75 km source and the sum of the kinetic (KE) and potential energy (PE) densities are shown in Figure 8 and are calculated using equations 8 and 9.

$$KE = (\bar{\rho}/4) * (|\hat{u}|^2 + |\hat{v}|^2 + |\hat{w}|^2) \quad (8)$$

$$PE = (\bar{\rho}/4) * (g/\omega_B)^2 (|\hat{\Theta}|^2/\Theta^2) \quad (9)$$

where  $\hat{u}$ ,  $\hat{v}$ , and  $\hat{w}$  are the complex amplitudes of the wave-induced zonal, meridional, and vertical wind perturbations,  $\bar{\rho}$  is the mean density,  $\hat{\Theta}$  is the complex amplitude of the wave induced potential temperature perturbation, and  $\Theta$  is the mean potential temperature. The total (kinetic plus potential) energy was  $\approx 10^{10}$  J.

[50] The energy deposited by an impulsive event would mainly go into high frequencies ( $>\omega_B$ ) because the energy is distributed over a broad range of frequencies and a greater range of frequencies is available at high rather than low frequencies. Likewise, a narrow, spatially localized disturbance such as a bolide will excite a broad range of horizontal wavenumbers. In addition, given that the frequency bandwidth of the disturbance is  $\approx \omega/n$  ( $n$  being the number of wave crests observed) an appreciable fraction of the energy deposited may go into exciting high frequency (i.e., large  $\omega$ ) waves with their comparatively large bandwidth. A similar bandwidth argument applies to the fairly large wavenumber disturbance we observe. Nevertheless, our analysis only

provides a rough estimate of the available energy and doubling the bolide radius, for example, would require only a small fraction of the deposition energy exciting our observed wave. Also, as noted above, acoustic energy can be detected at ground level from bolides that deposit their energy in the 90 km region.

[51] Thus, it is certainly possible, but speculative, that a Leonids meteor could have been the source of the observed wave. A more exact calculation would require a transient model that would also allow more realistic energy deposition based on a meteor losing its energy between 90 and 100 km.

## 5. Conclusions

[52] The major results of this study are as follows.

1. A wavelike oscillation was observed in images of the OHM airglow that had an observed period of  $\approx 215$  s and a horizontal wavelength of  $\approx 35$  km. The wave was travelling towards the southeast when it was observed over Starfire at approximately 10 UT on November 17th 1999.

2. This wave propagated faster, about 160 m/s, than any of the observed waves in recent airglow imaging studies.

3. The intrinsic properties of the wave were calculated using simultaneous wind and temperature data obtained from the Starfire Na lidar system. The wave appears to be external everywhere, except perhaps for narrow regions around 80 and 105–110 km.

4. A full-wave model analysis was used to calculate the wave induced temperature perturbations and wave energy. The temperature perturbations had a peak response near 85 km and near 110 km.

5. Based on both the WKB and full-wave analysis, these peaks may be related to the excitation of a Buoyancy or Lamb wave at those altitudes.

6. Based on the full-wave model analysis, it is suggested that the wave did not originate in the troposphere or stratosphere but more likely was generated in the upper mesosphere, perhaps by a Leonids meteor.

[53] **Acknowledgments.** Thanks to Dave Merriman for the considerable help given while the airglow imager was located at Starfire. We also thank Robert Fugate for allowing us to site the instrument at the Starfire facility. The Aerospace results could not have been obtained without the



invaluable help given by Kirk Crawford in all aspects of this project. J.H.H. and R.L.W. were supported by NSF grant ATM-9813834, NASA grant NAG5-9193, and by the Aerospace IR and D program. M.P.H. was supported by NSF grants ATM-9896276 and ATM-9816159. A.Z.L. was supported by NSF grant ATM97-09921.

## References

- Alexander, M. J., and L. Pfister, Gravity wave momentum flux in the lower stratosphere over convection, *Geophys. Res. Lett.*, **22**, 2029–2032, 1995.
- Baker, D., A. Steed, R. Huppi, and K. Baker, Twilight transition spectra of atmospheric O<sub>2</sub> IR emissions, *Geophys. Res. Lett.*, **2**, 235–239, 1975.
- Balachandran, N. K., Acoustic-gravity wave propagation in a temperature and wind-stratified atmosphere, *J. Atmos. Sci.*, **25**, 818–826, 1968.
- Beer, T., *Atmospheric Waves*, 300 pp., John Wiley, New York, 1974.
- Bills, R. E., C. S. Gardner, and C. Y. She, Narrow band lidar technique for sodium temperature and Doppler wind observations of the upper atmosphere, *Opt. Eng.*, **30**, 13–21, 1991.
- Chu, X., A. Z. Liu, G. Papen, C. S. Gardner, M. Kelley, J. Drummond, and R. Fugate, Lidar observations of elevated temperatures in bright chemiluminescent meteor trails during the 1998 Leonid shower, *Geophys. Res. Lett.*, **27**, 1815–1818, 2000.
- Clairemidi, J., M. Herse, and G. Moreels, Bi-dimensional observations of waves near the mesopause at auroral latitudes, *Planet. Space Sci.*, **33**, 1013–1022, 1985.
- Einaudi, F., and C. O. Hines, WKB approximation in application to acoustic-gravity waves, *Can. J. Phys.*, **48**, 1458–1471, 1970.
- Frey, H. U., S. B. Mende, J. F. Arens, P. R. McCullough, and G. R. Swenson, Atmospheric gravity wave signatures in the infrared hydroxyl OH airglow, *Geophys. Res. Lett.*, **27**, 41–44, 2000.
- Fritts, D. C., and L. Yuan, An analysis of gravity waves ducting in the atmosphere: Eckart resonances in thermal and Doppler ducts, *J. Geophys. Res.*, **94**, 8455–8466, 1989.
- Fritts, D. C., J. R. Isler, J. H. Hecht, R. L. Walterscheid, and Ø. Andreassen, Wave breaking signatures in sodium densities and OH nightglow, 2. Simulation of wave and instability structures, *J. Geophys. Res.*, **102**, 6669–6684, 1997.
- Garcia, F. J., M. J. Taylor, and M. C. Kelley, Two-dimensional spectral analysis of mesospheric airglow image data, *Appl. Opt.*, **36**, 7374–7385, 1997.
- Gardner, C. S., and G. C. Papen, Mesospheric Na wind/temperature lidar, *Rev. Laser Eng.*, **23**, 131–134, 1995.
- Georges, T. M., HF Doppler studies of travelling ionospheric disturbances, *J. Atmos. Terr. Phys.*, **30**, 735–746, 1968.
- Gossard, E. E., and W. H. Hooke, *Waves in the Atmosphere*, *Atmospheric Infrared and Gravity Waves—Their Generation and Propagation*, 456 pp., Elsevier Sci., New York, 1975.
- Hecht, J. H., R. L. Walterscheid, D. C. Fritts, J. R. Isler, D. C. Senft, C. S. Gardner, and S. J. Franke, Wave breaking signatures in OH airglow and sodium densities and temperatures, 1, Airglow imaging, Na lidar, and MF radar observations, *J. Geophys. Res.*, **102**, 6655–6668, 1997.
- Hecht, J. H., R. L. Walterscheid, M. P. Hickey, and S. J. Franke, Climatology and modeling of quasi-monochromatic atmospheric gravity waves observed over Urbana, Illinois, *J. Geophys. Res.*, **106**, 5181–5195, 2001.
- Hedin, A. E., Extension of the MSIS thermosphere model into the middle and lower atmosphere, *J. Geophys. Res.*, **96**, 1159–1172, 1991.
- Hedin, A. E., et al., Empirical wind model for the upper, middle, and lower atmosphere, *J. Atmos. Terr. Phys.*, **58**, 1421–1448, 1996.
- Hickey, M. P., R. L. Walterscheid, M. J. Taylor, W. Ward, Q. Schubert, G. Zhou, F. Garcia, M. C. Kelley, and G. G. Shepherd, Numerical simulations of gravity waves imaged over Arecibo during the 10-day 1993 campaign, *J. Geophys. Res.*, **102**, 11,475–11,489, 1997.
- Hickey, M. P., M. J. Taylor, C. S. Gardner, and C. R. Gibbons, Full-wave modeling of small-scale gravity waves using airborne lidar and observations of the Hawaiian airglow (ALOHA-93) O(<sup>1</sup>S) images and coincident Na wind, temperature lidar measurements, *J. Geophys. Res.*, **103**, 6439–6453, 1998.
- Hickey, M. P., R. L. Walterscheid, and G. Schubert, Gravity wave heating and cooling in Jupiter's thermosphere, *Icarus*, **148**, 266–281, 2000.
- Hickey, M. P., G. Schubert, and R. L. Walterscheid, Acoustic wave heating of the thermosphere, *J. Geophys. Res.*, **106**, 21,543–21,548, 2001.
- Hines, C. O., Internal atmospheric gravity waves at ionospheric heights, *Can. J. Phys.*, **55**, 441–445, 1960.
- Hines, C. O., Generalization of the Richardson criterion for the onset of atmospheric turbulence, *Q. J. R. Meteorol. Soc.*, **97**, 429–439, 1971.
- Isler, J. R., M. P. Taylor, and D. J. Fritts, Observational evidence of wave ducting and evanescence in the mesosphere, *J. Geophys. Res.*, **102**, 26,301–26,313, 1997.
- Jones, W. L., A theory for quasi-periodic oscillations observed in the ionosphere, *J. Atmos. Terr. Phys.*, **32**, 1555–1566, 1970.
- Krassovsky, V. I., Atlas of the airglow spectrum 3000–12400 Å, *Planet. Space Sci.*, **9**, 883–915, 1962.
- Nakamura, T., A. Higashikawa, T. Tsuda, and Y. Matsushita, Seasonal variations of gravity wave structures in OH airglow with a CCD imager at Shigaraki, *Earth Planets Space*, **51**, 897–906, 1999.
- Revelle, D. O., and R. W. Whitaker, Infrasonic detection of a leonid bolide: 1998 November 17, *Meteorit. Planet. Sci.*, **34**, 995–1005, 1999.
- Richardson, L. F., The supply of energy from and to atmospheric eddies, *Proc. R. Soc. London, Ser. A*, **67**, 354–373, 1920.
- Smith, S. M., M. Mendillo, J. Baumgardner, and R. R. Clark, Mesospheric gravity wave imaging at a subauroral site: First results from Millstone Hill, *J. Geophys. Res.*, **105**, 27,119–27,130, 2000.
- Swenson, G. R., R. Haque, W. Yang, and C. S. Gardner, Momentum and energy fluxes of monochromatic gravity waves observed by an OH imager at Starfire Optical Range, New Mexico, *J. Geophys. Res.*, **104**, 6067–6080, 1999.
- Taylor, M. J., and M. A. Hapgood, Identification of a thunderstorm as a source of short period gravity waves in the upper atmosphere nightglow emissions, *Planet. Space Sci.*, **36**, 975–985, 1988.
- Taylor, M. J., M. A. Hapgood, and P. Rothwell, Observations of gravity wave propagation in the OH(557.7 nm), Na(589.2 nm), and the near infrared OH nightglow emissions, *Planet. Space Sci.*, **35**, 413–427, 1987.
- Taylor, M. J., M. B. Bishop, and V. Taylor, All-sky measurements of short period gravity waves imaged in the OH(557.7 nm), Na(589.2 nm) and near infrared OH and O<sub>2</sub>(0,1) nightglow emissions during the ALOHA-93 campaign, *Geophys. Res. Lett.*, **22**, 2833–2836, 1995.
- Taylor, M. J., W. R. Pendleton, Jr., S. Clark, H. Takahashi, D. Gobbi, and R. A. Goldberg, Image measurements of short-period gravity waves at equatorial latitudes, *J. Geophys. Res.*, **102**, 26,283–26,299, 1997.
- Tsuda, T., M. Nishida, C. Roche, and R. H. Ware, A global morphology of gravity wave activity in the stratosphere revealed by the GPS occultation data (GPS/MET), *J. Geophys. Res.*, **105**, 7257–7274, 2000.
- Walterscheid, R. L., J. H. Hecht, R. A. Vincent, I. M. Reid, J. Woithe, and M. P. Hickey, Analysis and interpretation of airglow and radar observations of quasi-monochromatic gravity waves in the upper mesosphere and lower thermosphere over Adelaide, Australia (35° S, 138° E), *J. Atmos. Solar Terr. Phys.*, **61**, 461–468, 1999.

J. H. Hecht, R. J. Rudy, and R. L. Walterscheid, Space Science Applications Laboratory, The Aerospace Corporation, M2-259, P.O. Box 92957, Los Angeles, CA, 90009, USA. (james.hecht@aero.org; richard.rudy@aero.org; richard.walterscheid@aero.org)

M. P. Hickey, Department of Physics and Astronomy, Clemson University, 308 Kinard Laboratory, Clemson, SC 29634, USA. (hickey@hubcap.clemson.edu)

A. Z. Liu, Department of Electrical and Computer Engineering, University of Illinois, 308 C.S.L., 1308 W. Main Street, Urbana, IL, 61801, USA. (liuzr@uiuc.edu)